Evolution in the properties of Lyman-α emitters from redshifts $z \sim 3$ to $z \sim 2$[⋆]

K. K. Nilsson[1], C. Tapken[1], P. Møller[2], W. Freudling[2], J. P. U. Fynbo[3], K. Meisenheimer[1], P. Laursen[3], and G. Östlin[4]

[1] Max-Planck-Institut für Astronomie, Königstuhl 17, 69117 Heidelberg, Germany
   e-mail: knilsson@mpia-hd.mpg.de
[2] European Southern Observatory, Karl-Schwarzschild-Straße 2, 85748 Garching bei München, Germany
[3] Dark Cosmology Centre, Niels Bohr Institute, University of Copenhagen, Juliane Maries Vej 30, 2100 Copenhagen, Denmark
[4] Stockholm Observatory, Department of Astronomy, Stockholm University, AlbaNova University Centre, 106 91 Stockholm, Sweden

ABSTRACT

Context. Narrow-band surveys to detect Lyα emitters are powerful tools for identifying high, and very high, redshift galaxies. Although samples are increasing at redshifts $z = 3$–6, the nature of these galaxies is still poorly known. The number of galaxies detected at redshifts below $z \sim 3$ are also small.
Aims. We study the properties of $z = 2.25$ Lyα emitters and compare them with those of $z > 3$ Lyα emitters.
Methods. We present narrow-band imaging made with the MPG/ESO 2.2m telescope and the WFI (Wide Field Imager) detector. Using this data, we have searched for emission-line objects. We find 170 candidate typical Lyα emitters and 17 candidates that we regard as high UV-transmission Lyα emitters. We have derived the magnitudes of these objects in 8 photometric bands from u^* to K_s, and studied whether they have X-ray and/or radio counterparts.
Results. We demonstrate that there has been significant evolution in the properties of Lyα emitters between redshift $z \sim 3$ and $z = 2.25$. The spread in spectral energy distributions (SEDs) at the lower redshift is larger and we detect a significant AGN contribution in the sample. The distribution of the equivalent widths is narrower than at $z \sim 3$, with only a few candidates with rest-frame equivalent width above the predicted limit of 240 Å. The star formation rates derived from the Lyα emission compared to those derived from the UV emission are lower by on average a factor of ~1.8, indicative of a significant absorption by dust.
Conclusions. Lyα emitters at redshift $z = 2.25$ may be more evolved than Lyα emitters at higher redshift. The red SEDs imply more massive, older and/or dustier galaxies at lower redshift than observed at higher redshifts. The decrease in equivalent widths and star formation rates indicate more quiescent galaxies, with in general less star formation than in higher redshift galaxies. At $z = 2.25$, AGN appear to be more abundant and also to contribute more to the Lyα emitting population.

Key words. cosmology: observations – galaxies: high redshift

1. Introduction

Over the past decade, a large number of so-called Lyman-α (Lyα) emitters have been discovered at high redshift. Several techniques have been employed in the search for these galaxies, but the by far most common method is that of narrow-band imaging, where a narrow-band filter is tuned to Lyα within a particular narrow redshift range. Objects with large equivalent widths (*EW*s) are thus selected by comparing the colours in the narrow-band image and complementary broad-band images. Spectroscopically confirmed Lyα emitters now include several hundreds of sources at redshifts $z \sim 3$ (e.g., Møller & Warren 1993; Cowie & Hu 1998; Steidel et al. 2000; Fynbo et al. 2001, 2003a; Matsuda et al. 2005; Venemans et al. 2007; Nilsson et al. 2007; Ouchi et al. 2008), $z \sim 4.5$ (Finkelstein et al. 2007), $z \sim 5.7$ (Malhotra et al. 2005; Shimasaku et al. 2006; Tapken et al. 2006) and $z \sim 6.5$ (Taniguchi et al. 2005; Kashikawa et al. 2006). However, in the low redshift range, between $z \approx 1.6$ corresponding to the atmospheric cut-off in the UV and $z \sim 3$, little progress has been made. In practice, the lower redshift limit is in fact higher than $z \approx 1.6$ because of the drop-off in CCD sensitivity and a more typical lower redshift

limit is $z \sim 2.0$. Eight narrow-band surveys have so far been published below $z \sim 3$; Fynbo et al. (1999), Pentericci et al. (2000), Stiavelli et al. (2001), Fynbo et al. (2002, 2003a,b), Francis et al. (2004) and Venemans et al. (2007). Furthermore, Van Breukelen et al. (2005) published a sample of Lyα emitters (LAEs) at $z \sim 2.5$ using integral-field spectroscopy. The difficulty in observing the Lyα line between redshifts $2 < z < 3$ lies in the low throughput of optical systems, the low efficiency of CCDs in this wavelength range, and higher extinction in the atmosphere. Even so, the advantage of a smaller luminosity distance is rewarding in that a higher *flux* limit equals the same *luminosity* limit as surveys at higher redshift. It also facilitates follow-up observations into the nature of these objects.

At higher redshifts, Lyα emitters have been observed to be increasingly bluer, younger and smaller with increasing redshift. At $z \sim 3$, Gawiser et al. (2006) inferred stellar masses of a few $\times 10^8 \, M_\odot$, almost no dust extinction, and ages of the order of 100 Myr. In a follow-up paper, Gawiser et al. (2007) studied a stacked sample of 52 Lyα emitters without Spitzer detections and confirmed their results of young ages and that no dust appears to be present in these systems, although they inferred slightly higher masses. The galaxies in their sample with Spitzer detections are presented in Lai et al. (2008). For these galaxies, older ages and higher masses are reported and the authors

---

[⋆] Full Table 2 is only available in electronic form at
http://www.aanda.org

Table 1. Log of imaging observations with WFI.

Date	Total exp.	Average seeing
10–11.03.2007	0.56 h	1''40
11–12.03.2007	0.83 h	1''24
12–13.03.2007	1.33 h	1''04
13–14.03.2007	2.50 h	1''65
14–15.03.2007	1.67 h	1''26
15–16.03.2007	1.45 h	1''81
16–17.03.2007	3.33 h	1''11
17–18.03.2007	1.67 h	1''32
18–19.03.2007	3.33 h	1''15
19–20.03.2007	2.50 h	1''25
20–21.03.2007	2.50 h	1''36
22–23.03.2007	1.67 h	1''13

Fig. 1. Transmission of selection filters. The WFI narrow-band filter is drawn with a solid line. The dashed line shows the SUBARU *Bj* band filter curve and the dotted line the CFHT *u** band filter curve.
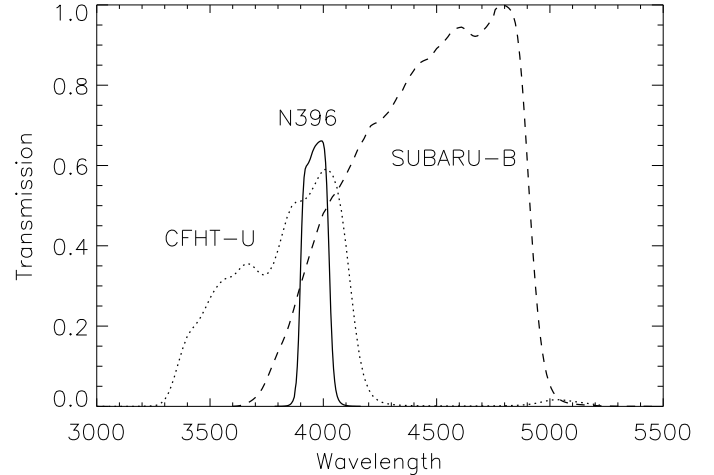
propose that $z \sim 3$ Lyα emitters may have a wide range of properties. In Nilsson et al. (2007), a stacked sample of Lyα emitters at $z = 3.15$ were studied. Here, small masses and low dust contents were inferred, but the ages were unconstrained. At even higher redshift, Pirzkal et al. (2007) showed that a sample of $4 < z < 5.7$ Lyα emitters had very young ages of a few Myr and small stellar masses, in the range 10^6–10^8 $M_\odot$. These results agreed well with those of Finkelstein et al. (2007), who studied almost 100 Lyα emitters at $z = 4.5$. Finkelstein et al. (2008) reported, studying a different sample, finding very dusty, massive galaxies with A_{1200} as high as 4.5 mag and masses as high as several $\times 10^{10}$ $M_\odot$, at $z = 4.5$. They argued that they observed a bimodality in the properties of Lyα emitters; young and blue galaxies versus old and dusty. Thus, the properties of $z \geq 3$ Lyα emitters are poorly constrained, but these galaxies tend to be considered young, blue, small and dust-free. With the data presented here, we aim to extend the study of the properties of Lyα emitters to lower redshifts, where a wider range of the SED can be studied in the optical/infrared and the luminosity distance is smaller, allowing a more detailed analysis.

This paper is organised as follows. Section 2 presents the observations leading to our sample, as well as the data reduction. Section 3 includes the object detection and candidate selection and a discussion about possible interlopers in the sample. In Sect. 4 we present all the basic characteristics of the sample, including photometry, AGN contribution, surface density, and sizes, and the equivalent width distribution of the candidates. We summarise the results in Sect. 5.

Throughout this paper, we assume a cosmology with $H_0 = 72$ km s^{-1} Mpc^{-1} (Freedman et al. 2001), $\Omega_m = 0.3$ and $\Omega_\Lambda = 0.7$. Magnitudes are given in the *AB* system.

2. Observations

In March 2007, a 35×34 arcmin^2 section of the COSMOS field, centred on RA = $10^h00^m27^s$ and Dec = $02°12'22''7$ (J2000), was observed with the Wide-Field Imager (WFI; Baade et al. 1999) on the MPG/ESO 2.2 m telescope on La Silla. A log of the observations can be found in Table 1. The total dithered image consisted of 29 exposures with a total exposure time of 99 624 s, or 27.7 h. The observations were made with narrow-band filter N396/12 with a central wavelength of 396.3 nm and a *FWHM* of 12.9 nm. This wavelength range corresponds to $z = 2.206$–2.312 for Lyα, $z = 0.046$–0.081 for [OII], and $z = 1.52$–1.59 for CIV and the surveyed comoving volumes (after masking, see Sect. 3.1) are $\sim$329 300 Mpc^{-3}, 820 Mpc^{-3} and $\sim$225 000 Mpc^{-3}, respectively. The narrow-band filter curve is

shown with the filter curves of the filters used for the selection of candidates in Fig. 1.

The data were reduced using the *MPIAphot* pipeline developed in MIDAS with specific routines to handle WFI data. We briefly describe the reduction steps performed on the data. The data from the individual CCDs were converted into MIDAS format and bias-corrected on each separate CCD. The individual CCD frames were then placed into placeholders in an empty mosaic, thus creating a full mosaic for each frame including the gaps between the CCDs. To correct for bad pixels and columns as well as correcting columns with a constant offset compared to the surrounding pixels, lamp images with exposure times ranging between 1–220 s were downloaded and analysed. The science frames were then corrected for both the bad columns and the offset columns. The frames were then flat-field corrected using a master flat created from sky flats taken at the time of observations. To determine the offsets between the images, an SDSS catalogue of known sources was used, combined with an algorithm that identifies sources and matches them with catalogue entries. The information about the shift is then entered into the header. In the final step, the images were shifted and rebinned onto a gnomonic projection (i.e. by de-projecting all great circles onto straight lines), cosmic-ray hits were removed and a final, co-added image created. Significant residuals from the background subtraction were apparent in the mosaiced image, in particular around the edges of the individual images used to create the mosaic. We used the following procedure to remove it. First, we used the "clean" option of the IRAF task *imsurfit* to create a version of the image in which objects had been removed and interpolated over. We then edited this image interactively to remove any residual flux from objects. Subsequently, we fitted a 20×20 piece bicubic spline to this image. We then subtracted this fit from the original image. This procedure reduced the background variations to a small fraction of the background noise. We then flux calibrated the narrow-band image by calculating the fluxes of all narrow-band selected objects (see Sect. 3.1) in the CFHT *u** and the SUBARU *Bj* images (see Table 3) and interpolated the fluxes in the narrow-band image. We can then calculate the zero-point of the image, assuming that the median equivalent width of all objects is zero. The 5σ detection limit in a 3'' diameter aperture in the image is 25.3 *AB*

magnitude and the 90% completeness limit is 25.1 *AB* magnitude, corresponding to Lyα luminosities of $\log L = 42.36$ erg s^{-1} and $\log L = 42.44$ erg s^{-1}, respectively, at $z = 2.25$.

3. Selection of candidates

3.1. Object detection and candidate selection

For object detection, we used the SExtractor software (Bertin & Arnouts [1996](#)). The narrow-band image was used as a detection image, and objects with a minimum of 8 adjoining pixels and a threshold of 2σ per pixel were selected. For the selection, we used two broad-band filters corresponding to wavelengths to both the blue and red side of the narrow-band filter, the CFHT u^* band image and the SUBARU *Bj* band image, see also Fig. [1](#). Both images were taken from the public data in the COSMOS field (Capak et al. [2007](#)). The u^* and *Bj* band images were created from combining several smaller sub-images to match perfectly the field of the narrow-band image, and they were subsequently re-binned and smoothed to match the pixel size and source PSF of the narrow-band image. The flux of each object detected in the narrow-band image was then measured in all three bands in circular apertures with a diameter of 3″, where each aperture was centred on the position of the object detected in the narrow-band image. For the catalogue, we included only objects with $S/N > 5$ in the narrow-band image that were found at least 70 pixels from the edge of the image. We also masked areas where stray light and bright stars affected the image. This left us with a catalogue of 21 275 objects in an effective area of $\sim$1014 arcmin^2.

The candidate Lyα emitters were selected according to a similar method as described in Nilsson et al. ([2007](#)). The method is based on determining the equivalent width (*EW*) of a potential emission/absorption line located in the narrow-band wavelength range. Thus, the flux density was determined in the CFHT u^* and SUBARU *Bj* bands and interpolated between the central wavelengths of these filters and the central wavelength of the narrow-band filter. The *EW* was then determined by dividing the measured flux in the narrow-band with the interpolated flux density. Simultaneously, we also calculated the propagated statistical error in this measurement. The calculated *EW* represents a lower limit to the true *EW* of the object as there may be several objects, unrelated to the narrow-band object, detected inside the aperture in the broad-band images. The *EW* calculation is also complicated by the uncertainties in the continuum interpolation (Hayes & Östlin [2006](#); Hayes et al. [2008](#)). To compile the final catalogue of Lyα emitting candidates, we used two selection criteria. First, all objects with a measured *EW* larger than or equal to 65 Å (corresponding to 20 Å in the restframe for Lyα) are selected. To further exclude false candidates at the faint magnitude end of the sample, in which the *EW* measurement is dominated by the broad-band flux uncertainties, a significance of the *EW* greater than 2.3 is required. These criteria are designed to detect all emission-line objects with large equivalent widths accurately. This final catalogue includes 386 objects. Following the procedure of Fynbo et al. ([2002](#)), three co-authors then individually ranked these 386 candidates by visual inspection into three categories; first a category of rejected detections (caused by CCD or stellar artifacts or enhancement due to airplane/satellite tracks), then into two categories of likely candidates and candidates that are unlikely to be real but for which no obvious reason was found to reject them (see also Fig. [2](#)). The 386 candidates were split into the different categories of [Likely, Unlikely, Rejected] = [187, 61,
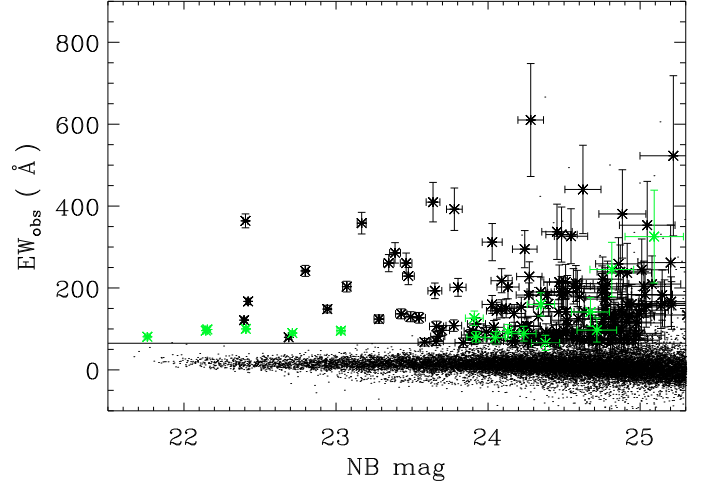

Fig. 2. Plot of the selection criteria, with narrow-band magnitude on the *x*-axis and observed equivalent width on the *y*-axis. Selected candidates are shown with error bars, green points correspond to the GALEX-detected objects, see Sect. [3.2](#). Solid line marks the 65 Å limit. Objects above this line with *EW* significance greater than 2.3σ are selected in the first catalogue. Dots mark the entire sample of 5σ detections in the narrow-band, and dots above the selection criteria without error bars were rejected in the visual inspection.
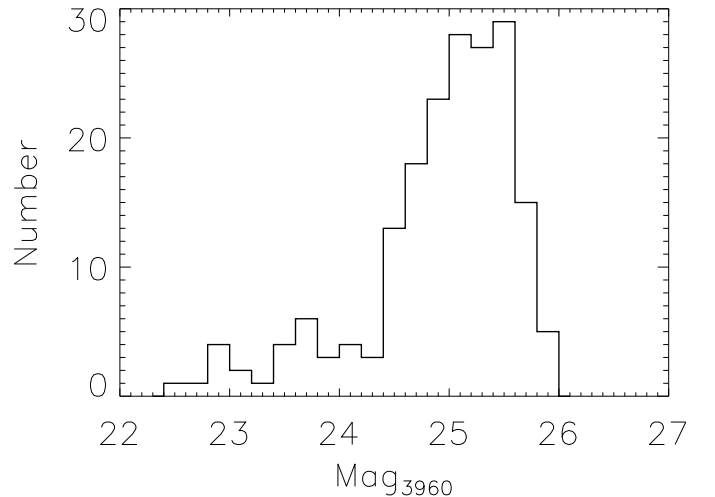

Fig. 3. Histogram of Lyα magnitudes (continuum-subtracted narrow-band magnitudes), Mag$_{3960}$, of emission-line candidate sample. Binsize is 0.2.

138]. In Table [2](#), we list the coordinates, *EW*s, significance of the *EW*s, continuum-subtracted narrow-band magnitudes Mag$_{3960}$ and mean UV spectral index β (see Sect. [4.1](#)) of all likely candidates (coordinates of unlikely candidates may be obtained from the authors). In the following sections, we only include the candidates in the likely category, which provides a total of 187 candidates. The Lyα magnitudes of our LAE candidates are given by the range Mag$_{3960}$ = 22.57−25.88 corresponding to Lyα luminosities in the range of $\log L_{Ly\alpha}$ = 42.13−43.45 (see also the histogram of magnitudes in Fig. [3](#)).

3.2. Interloper discussion

The only possible contaminants in the sample are [OII] emitters at $z = 0.06$ and CIV emitters at $z = 1.56$. For [OII] emitters at this redshift, the detection limit corresponds to a luminosity limit

Table 2. Coordinates, observed equivalent widths, continuum subtracted narrow-band magnitudes and UV spectral index β of the candidates. Full table is available in the online version.

			Rank 1 candidates			
LAE_COSMOS_#	RA	Dec	EW (Å)	Mag$_{3960}$	β	
1	150.05310	1.94797	142.7 ± 38.6	25.50 ± 0.34	-0.48 ± 0.24	
2	150.21068	1.95100	225.8 ± 57.0	25.41 ± 0.32	-0.82 ± 0.33	
3	150.29437	1.95107	564.0 ± 43.2	24.24 ± 0.09	-1.40 ± 0.40	
4	150.25458	1.95224	118.4 ± 33.4	25.55 ± 0.36	-2.12 ± 0.33	
5	150.31830	1.95244	279.3 ± 41.8	24.91 ± 0.18	-2.08 ± 0.44	
6	150.37505	1.95619	95.9 ± 24.2	25.46 ± 0.32	-1.84 ± 0.29	
7	150.15936	1.95717	790.3 ± 140.1	25.04 ± 0.21	-2.97 ± 1.06	
8	150.37990	1.96143	119.6 ± 16.8	24.88 ± 0.16	1.81 ± 0.22	G
9	150.28378	1.96167	248.1 ± 50.2	25.20 ± 0.25	-1.84 ± 0.34	
10	150.30785	1.96243	81.0 ± 28.5	25.80 ± 0.47	0.54 ± 0.26	

Coordinates are in J2000. Candidates marked with the capital letter G are detected with GALEX, see text below.

of $\log L = 38.7$ erg s^{-1} and the survey volume is 820 Mpc^{-3}. For CIV emitters, the corresponding limit is $\log L = 42.0$ erg s^{-1} and the survey volume is ~225 000 Mpc^{-3}. Unfortunately, no published luminosity function for local Universe [OII] emitters or CIV emitters reach these faint luminosity limits, but for [OII] emitters, extrapolating from the luminosity functions of Hogg et al. (1998), Gallego et al. (2002), and Teplitz et al. (2003), we conclude that we could expect between a few to 200 [OII] emitters in the survey volume. To constrain this value further, the [OII] luminosity function was extrapolated from the Hα luminosity function of Ly et al. (2007). Assuming a conversion between [OII] and Hα luminosities given by the star formation rate equations of Kennicutt (1998) and Kewley et al. (2004), the [OII] luminosity limit corresponds to an Hα luminosity limit of $\log L = 38.8$ erg s^{-1} in this survey. To this limit, Ly et al. (2007) detected ~0.2 emitters per Mpc^{-3}, corresponding to approximately 160 objects in our survey volume, of which only 2% are expected to have an EW larger than the selection criteria limit of $EW_{\mathrm{obs}} = 65$ Å (Hogg et al. 1998). Based on the results of Ly et al. (2007), approximately three [OII] emitters are hence included in the list of candidates.

We also extracted the photometric redshifts for our candidates from the catalogue of Gabasch et al. (2008). The catalogue is incomplete in areal coverage and covers roughly 80% of our field. The catalogue was searched for counterpart objects within a 2″ radii from the position of our source. If several objects were found, the object nearest to our source was chosen as the counterpart. For a total of 187 candidates, 132 had detected counterparts. Unfortunately, the near-IR coverage of the COSMOS field is patchy and shallow, which complicates any photometric redshift determination in the redshift range $z \sim 1.3-2.5$, since in this range the Lyman-break has not yet entered the optical window and the Balmer break is in the near-IR. This means that we are in principle able to exclude [OII] emitters from the sample, whereas other intermediate redshift emitters, such as CIV, are difficult to exclude. The redshifts of our 132 detected candidates also show that no emitters are consistent with being [OII] emitters, and the median redshift of the candidates is $z = 1.7$, with most of the candidates being consistent with having a redshift of $z = 2.25$ to within 3σ margins of error. To study how many CIV emitters may be expected in the survey volume, we used the AGN luminosity function of Bongiorno et al. (2007). Since CIV emission of restframe equivalent widths larger than $EW_0 \gtrsim 25$ are only expected to originate in AGN, and with the luminosity limits in the optical of this survey, the expected number of CIV

emitters in our survey volume is ~2. Any contamination of CIV emitters in the total sample of candidates is thus minimal.

The COSMOS field also has publicly available GALEX near- and far-UV data. This data may be used to exclude any remaining [OII] emitters from the sample, since the limiting magnitude of the GALEX data is ~25.5 in the NUV band and, assuming a flat spectrum, all [OII] emitters in the sample should be detected in the GALEX data based on the flux limit in the Bj band. Lyα emitters may or may not be detected in the GALEX data, depending on the level of absorption from the Lyman forest. Lyα emitters would require a transmission of less than 60% to be undetected in the GALEX images. Møller & Jakobsen (1990) inferred that approximately 10% of galaxies at redshift $z = 2.25$ have transmissions in the UV higher than 60%, in agreement with recent observations at $z \sim 1.5$ (Siana et al. 2007). The conclusion is that we expect all [OII] emitters to be detected in the GALEX images, whereas the total sample of GALEX-detected objects is a mix of high transmission Lyα emitters and [OII] emitters. Of the 187 candidates, 17 are detected in the GALEX images (labelled by a G in Table 2). The largest EW of a GALEX-detected candidate is $EW_{\mathrm{obs}} = 604$ Å. As shown earlier, the expectation is ~3 [OII] emitters in the survey volume, and so most of the GALEX-detected objects are most likely to be high transmission Lyα emitters. We separate the GALEX-detected sample and the non-GALEX-detected sample in the following analysis. Thus, we have two samples; one robust sample of 170 Lyα emitter candidates (removing 17 GALEX detections from a total of 187 candidates), which is expected to be free of interlopers, and one sample of 17 GALEX-detected objects, possibly including a small contamination of [OII] emitters but consisting mostly of high-transmission Lyα emitters. The non-GALEX-detected sample is a conservatively selected sample defined so that the probability of having non-LAE objects in it is minimal, but at the price that it is less complete. For this reason, it is unsuitable for determining volume and surface densities. In Sect. 4.3 we return to this issue and define a sample suited for this purpose. From here on, whenever the "sample" is mentioned it is referring to the non-GALEX-detected sample.

4. Basic characteristics of LAEs

4.1. Photometry

For the photometry of the candidates, we use the public data-set from the COSMOS survey (Capak et al. 2007). The photometry presented here has been made in the bands found in Table 3.

Table 3. COSMOS broad-bands used.

Band	Observatory	CWL (Å)	$FWHM$ (Å)	Depth
u^*	CFHT	3798	720	26.4
Bj	SUBARU	4460	897	27.3
g^+	SUBARU	4780	1265	27.0
Vj	SUBARU	5484	946	26.6
r^+	SUBARU	6295	1382	26.8
i^+	SUBARU	7641	1497	26.2
z^+	SUBARU	9037	856	25.2
K_s	KPNO	21500	3200	21.6

The depths are 5σ AB magnitudes as measured in 3″ apertures (Capak et al. 2007).

All images are on the common COSMOS tiling grid and were cut and re-binned to match the narrow-band image in coverage and pixel size. We ran SExtractor in dual image mode, measuring the flux in apertures defined in the narrow-band image, also including the RMS images in the measurement through the WEIGHT_IMAGE option. The apertures had a diameter of 3″. Magnitudes were calculated using the zero-point given in the COSMOS data release. These magnitudes will, in the case of the candidates, be underestimated, since objects unrelated to the LAE candidate may be blended into the aperture (see below for a discussion of contamination in the aperture). In the following we exclude the results in the g^+ band as these magnitudes appear to be inconsistent. When plotting the SEDs of the objects, the g^+ band magnitudes are consistently lower than the other SED points by 0.1−0.5 mag.

We calculated the UV spectral index of β for the candidates, which is defined to be:

$$f_\lambda \propto \lambda^\beta \qquad (1)$$

where f_λ is the flux density per wavelength interval in the UV range. The spectral index is calculated as in Meurer et al. (1997) and Hathi et al. (2008) for the Bj, Vj, and r^+ bands using the following equations:

$$\beta_{Bj-Vj} = 4.456 \times (Bj - Vj) - 2 \qquad (2)$$

$$\beta_{Bj-r^+} = 2.673 \times (Bj - r^+) - 2 \qquad (3)$$

where Bj, Vj, and r^+ are the AB magnitudes in the respective bands. A plot of the results can be seen in Fig. 4 and the total β, calculated to be the mean of the two measurements as described in Eqs. (2) and (3), for our LAE candidates is found in Table 2. Most of the candidates are within the expected range of $-2 < \beta < 0$, with some outliers at both larger and smaller β. Of the four objects with $\beta_{Bj-Vj} \geq 2$, one is also detected in the K_s images, and two are affected by contamination from nearby objects. These objects are in the mid range of narrow-band magnitude, but in general have higher fluxes in the Vj band. On the other end of the scale, the three objects with $\beta_{Bj-Vj} \leq -4$ are all drawn from the faint end of the magnitude distribution in both the narrow-band and the Vj band, which explains their large error bars.

The SEDs of the candidates have characteristics that are atypical of higher redshift LAE SEDs. It has previously been reported that LAEs have SEDs that are in many cases blue (Gawiser et al. 2006, 2007; Pirzkal et al. 2007). Only two other surveys reported detections of red SEDs in several LAEs (Stiavelli et al. 2001; Lai et al. 2008), although one extremely red object was found by Nilsson et al. (2007). Among the 170 objects detected in this survey, a total of 118 candidates have
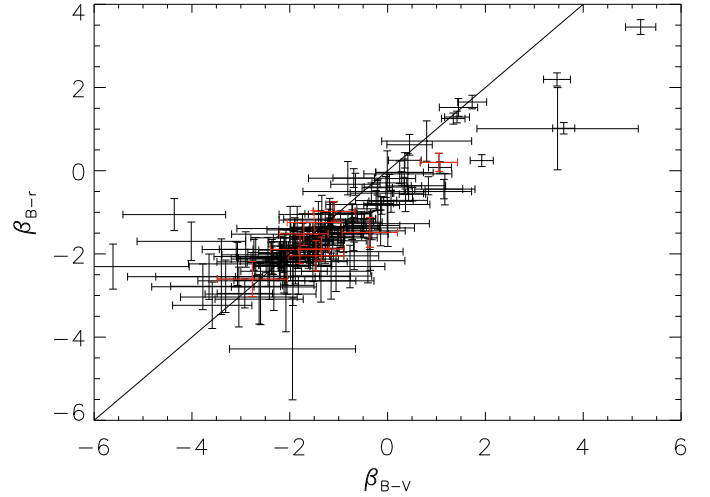

Fig. 4. UV spectral index calculated from the $Bj-Vj$ and $Bj-r^+$ colours. The two colours give approximately the same results, as seen by the solid line marking a linear relation. The spread in the spectral index is very large. AGN (see Sect. 4.2) are marked in red. Objects with red SEDs can be found in the upper right corner and objects with blue SEDs in the lower left corner.
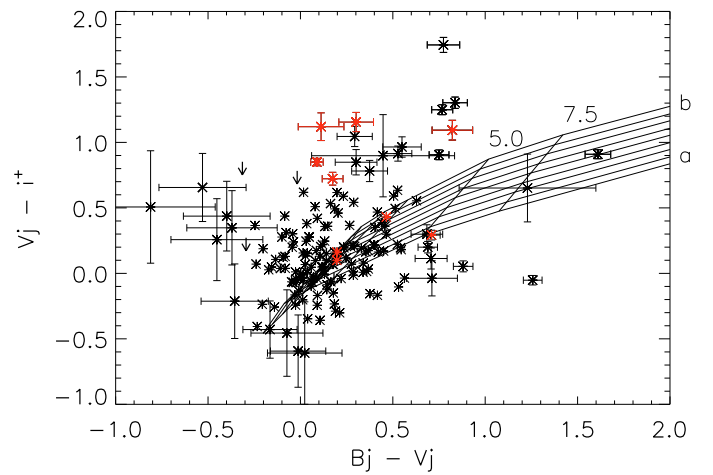

Fig. 5. Colour–colour diagram with $Bj - Vj$ on the x-axis and $Vj - i^+$ on the y-axis. Objects with upper limits (on the flux) in one band are shown as arrows with 3σ upper limits and objects with a colour in either bands that is 1.5σ away from the median colour in that band are shown with error bars. AGN are marked in red. The solid lines display the evolution of a single stellar population with increasing dust and age; age causes the objects to move predominantly to the right in the plot and dust predominantly upwards. The markers 5.0 and 7.5 correspond to age steps of 5.0×10^8 and 7.5×10^8 yrs and the dust steps go from $E(B - V)$ of 0.0 (point a in the plot) to 1.0 (point b in the plot) in steps of 0.125.

$Vj - i^+$ colours greater than zero, indicative of red colours, and five candidates have undefined colours due to upper limits in both bands, or only in the i^+ band. The median values of $Bj - Vj$ and $Vj - i^+$ among candidates with 3σ detections in both bands is 0.14 and 0.15, respectively. In Fig. 5, the colours $Bj - Vj$ and $Vj - i^+$ are plotted in a colour-colour diagram. In this figure, the tracks of a single stellar population, with increasing age and dust content, are superimposed. These populations were simulated with GALAXEV (Bruzual & Charlot 2003) in age steps of 1, 10, 50, 100, 500 and 750 Myr and 1 and 2 Gyr. The dust extinction was increased in 9 steps of $E(B - V)$ between 0.0 and 1.0 with

Table 4. Stacked magnitudes for the sample.

	Total sample	Red sample	Blue sample	K_s-detected
u^*	25.21 ± 0.03	25.16 ± 0.05	25.34 ± 0.06	24.75 ± 0.06
Bj	25.14 ± 0.03	25.11 ± 0.04	25.34 ± 0.05	24.00 ± 0.02
Vj	24.99 ± 0.08	24.89 ± 0.11	25.18 ± 0.03	23.04 ± 0.01
i^+	24.95 ± 0.14	24.72 ± 0.13	25.37 ± 0.15	21.83 ± 0.01
z^+	24.86 ± 0.22	24.57 ± 0.15	25.40 ± 0.16	21.46 ± 0.01
K_s	24.00 ± 0.29	23.65 ± 0.19	$25.55 \pm 0.98^*$	20.44 ± 0.02

Upper limits are 3σ. K_s-detected sample is without AGN-detected galaxies. *Blue sample K_s magnitude is calculated from the K_s magnitudes of the total and red samples.

increments of 0.125 using the Calzetti extinction law (Calzetti et al. 2000). We also completed simulations of an exponentially decaying star formation rate (SFR) and constant SFR. However, the colours of these populations occupy a smaller region of the diagram than those of the single stellar populations and were omitted from the plot. Most of the candidates are consistent with being young galaxies with ages in the range 10^6–10^8 yrs with various dust contents. Some objects appear evolved with a range of dust content. There are also some objects that appear evolved but fall below even the zero-dust line in the plot, which may be affected by nearby objects. Another group of objects are very red in terms of their $Vj - i^+$ colours but are too blue in $Bj - Vj$ to be explained by simple stellar populations. These may be reproduced more accurately by models with more complicated star formation histories.

In the sample, 12 objects have K_s band detections above the limiting magnitude of 22.2 (3σ, AB), corresponding to 7% of the complete sample. Note that four of these 12 K_s-detected objects are also selected as AGN (see Sect. 4.2). The K_s-detected objects are all drawn from the brighter end of the candidate sample, but have a range in Vj magnitude of 21.5–26, whereas the entire candidate sample have a range in magnitude of 21.5–27, i.e. not only the brightest candidates have K_s detections. We stacked the thumb-nail images of the candidates without K_s detections, removing objects from the stack with nearby, unrelated, bright detections. The total stack consisted of 144 candidates (with GALEX detections and objects with nearby, unrelated detections removed) and revealed a mean detection in the sample of magnitude 24.00 ± 0.29. The sample was also divided into two subsamples with $Vj - i^+$ colours $Vj - i^+ \geq 0$ and $Vj - i^+ < 0$, respectively. In the subsample with red $Vj - i^+$ colours, consisting of 96 of the 144 candidates, a clear detection with magnitude 23.65 ± 0.19 was made. In the subsample with bluer colours, no detection was made and an upper limit of 24.26 (3σ) was derived. In Fig. 6, we show the stacked magnitudes of the sample divided into four bins; the total sample, the sample with $Vj - i^+ \geq 0$ (called the "red" sample), the sample with $Vj - i^+ < 0$ (called the "blue" sample), and the K_s-detected sample. The total sample consists of 144 candidates, the red subsample consists of 96 candidates, and the blue subsample consists of 48 candidates. The magnitudes in Fig. 6 are also found in Table 4. In Fig. 6, it is seen that the stacked SED of the total sample is redder than those at $z \sim 3$; the points of the non-K_s-detected galaxies are in principle consistent with the Nilsson et al. (2007) fit within 2σ but inconsistent across the spectrum with the Gawiser et al. (2007) fit. The normalised K_s magnitude for the total sample is 25.45 ± 0.29, whereas the same magnitudes measured from the synthetic SEDs of Nilsson et al. (2007) and Gawiser et al. (2007) are 26.00 and 26.39, respectively. Hence, roughly two-thirds of the entire sample exhibit on average more red SEDs than at $z \sim 3$. Noteworthy
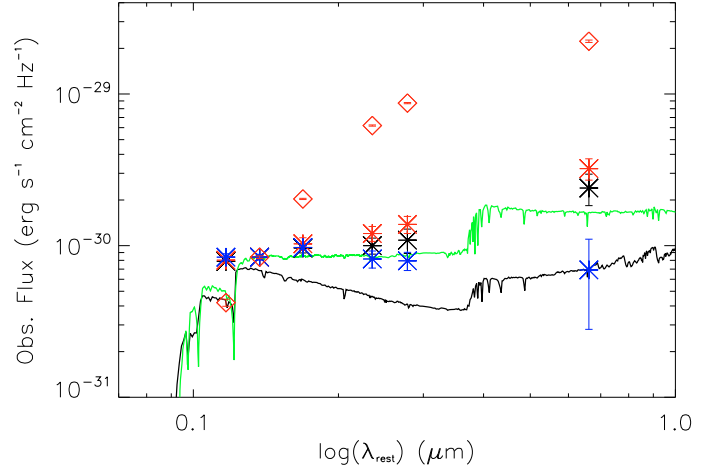

Fig. 6. Stacked SED of the sample. Points are the stacked magnitudes in six bands (u^*, Bj, Vj, i^+, z^+ and K_s) and in three bins; black points are the full sample, excluding K_s-detected galaxies and galaxies with bright nearby objects, red stars are those with red $Vj - i^+$ colours and blue points those with blue $Vj - i^+$ colours. Red diamonds mark the stacked K_s-detected sample without AGN-detected galaxies. All are normalised to the Bj flux of the Nilsson et al. (2007) SED. The lines are two best-fit SEDs of $z \sim 3$ LAEs from Nilsson et al. (2007, green line) and Gawiser et al. (2007, black line).

is also that SED of the blue sample (with $Vj - i^+ < 0$) is consistent with the $z \sim 3$ SEDs. The $Vj - K_s$ slopes of the red and blue samples are 1.24 ± 0.22 and -0.37 ± 0.98, indicating a clear difference in the properties of the blue and red samples of galaxies. For reference, the $Vj - K_s$ slope of the K_s-detected sample is 2.68 ± 0.04. A large spread in colours is evident in this survey, from the "classical" blue, flat SED galaxies to galaxies with very red SEDs, where the redder SEDs constitute two-thirds of the sample (see also Finkelstein et al. 2008, for a similar result). In a future paper, the Spitzer fluxes of these galaxies will be studied.

To study the level of contamination in the apertures, and the possibility that the very red SEDs originate from this source, the narrow-band catalogue was searched for other detected objects within two aperture radii (i.e. within 3″) of each LAE candidate. Of the 170 non-GALEX-detected candidates, 26 have one or more detected objects within this search radius. This corresponds to a potential contamination rate of 15% in the photometric measurements. Two objects have more than one nearby object. We also wish to determine if the apparent high number of red objects is caused by flux contamination from unrelated objects in the aperture. Of the 26 candidates with nearby objects, 19 have a $Vj - i^+$ colour in the aperture greater than zero, and 15 have $Vj - i^+$ colours larger than the median of $Vj - i^+$ for all 170 candidates. This implies that the contamination is not confined to only apparent red objects but affects all types of SEDs. We are thus confident that the contamination in the photometry is small, and that contamination cannot explain the apparent red colours of the LAE candidates.

4.2. AGN contribution

The COSMOS public data includes a release of X-ray data in three bands, 0.5–2.0, 2.0–4.5, and 4.5–10.0 keV, as observed by the XMM observatory (Hasinger et al. 2007). We used the catalogue of objects of Cappelluti et al. (2007) to measure the AGN fraction of all candidates. The catalogue consists of 1390 entries representing point-like sources and gives the fluxes in the three

Table 5. X-ray and radio properties of counterparts of the candidates.

LAE_COSMOS_#	$S_{0.5-2.0}$	$S_{2.0-4.5}$	$S_{4.5-10.0}$	*HR1*	*HR2*	$\log(L_{0.5-2.0})$	Offset (X-ray)	$S_{1.4\,\mathrm{GHz}}$	Offset (Radio)
				LAE candidates					
25	129.0 ± 1.87	191.0 ± 5.63	133.0 ± 7.03	0.19 ± 0.01	-0.18 ± 0.03	45.67 ± 0.02	11.06	—	—
36	—	—	—	—	—	—	—	140 ± 27	0.10
57	—	—	—	—	—	—	—	47 ± 10	6.17
82	1.25 ± 1.97	—	—	<0.52	—	43.66 ± 0.41	1.07	—	—
101	—	—	—	—	—	—	—	137 ± 27	0.06
113	1.21 ± 4.10	9.58 ± 29.1	—	0.78 ± 0.61	<0.01	43.64 ± 0.64	10.55	—	—
115	7.20 ± 6.00	16.2 ± 21.5	—	0.38 ± 0.59	<-0.25	44.42 ± 0.78	0.17	—	—
119	0.92 ± 0.26	—	—	<0.63	—	43.55 ± 0.14	2.67	—	—
121	17.6 ± 0.73	31.0 ± 2.54	18.3 ± 3.52	0.28 ± 0.04	-0.26 ± 0.11	44.81 ± 0.03	6.36	—	—
129	1.10 ± 0.27	—	—	<0.57	—	43.60 ± 0.12	1.95	—	—
132	—	—	—	—	—	—	—	47 ± 10	9.83
140	17.5 ± 0.72	46.3 ± 2.97	44.9 ± 4.73	0.45 ± 0.03	-0.02 ± 0.06	44.80 ± 0.02	0.74	—	—
150	2.6 ± 0.30	8.3 ± 1.48	—	0.52 ± 0.07	<0.08	43.98 ± 0.05	0.62	107 ± 30	0.21
161	2.42 ± 0.33	—	—	<0.25	—	43.95 ± 0.06	0.21	—	—
				GALEX-detected candidates					
42	4.9 ± 2.92	—	—	<-0.10	—	40.6 ± 0.39	0.55	—	—
108	8.3 ± 0.60	16.9 ± 2.14	—	0.34 ± 0.06	<-0.27	40.83 ± 0.03	1.01	—	—
126	7.9 ± 0.50	12.0 ± 1.79	—	0.38 ± 0.59	<-0.11	40.81 ± 0.03	0.45	—	—
155	3.0 ± 0.34	5.6 ± 1.21	—	0.30 ± 0.10	<0.27	40.39 ± 0.06	1.57	—	—
173	—	—	—	—	—	—	—	110 ± 25	9.44

Data from the catalogues of Cappelluti et al. (2007) and Schinnerer et al. (2007). X-ray fluxes are given in units of 10^{-15} erg s^{-1} cm^{-2} and radio fluxes in units of μJy. *HR1* and *HR2* correspond to the hardness ratios defined in Eqs. (4) and (5). The X-ray luminosity is in erg s^{-1}, assuming the objects are located at redshifts $z = 2.25$ and 0.06 for LAE and GALEX-detected candidates respectively. Offsets are distance from centroid of narrow-band detection to X-ray/radio detection in units of arcseconds. It is expected that the objects with offsets larger than a few arcseconds (25, 57, 113, 121, 132 and 173) are unrelated to the candidates due to the large offset and the relatively large probability of random association.

bands including errors. The catalogue detects objects to limiting fluxes of 7.2×10^{-16}, 4.0×10^{-15}, and 9.7×10^{-15} erg s^{-1} cm^{-2}, respectively, in the bands $0.5-2.0$, $2.0-4.5$, and $4.5-10.0$ keV with a confidence of roughly 4.5σ (Hasinger et al. 2007). This catalogue was searched for objects detected within a radius of $8''$ (i.e. 2 pixels in the XMM images) of the candidates. Fifteen of these potential counterparts were detected, of which five were from the list of GALEX-detected candidates. The X-ray fluxes of these candidates are found in Table 5. Note that the probability of finding an X-ray object within an aperture of radius $8''$ is ~ 0.009, resulting in potentially two random detections in the combined GALEX and non-GALEX-detected sample. For the objects with detections in two or all bands, the hardness ratios can be calculated. Hardness ratios are defined to equal:

$$HR1 = (S_{2.0-4.5} - S_{0.5-2.0}) / (S_{2.0-4.5} + S_{0.5-2.0}) \quad (4)$$

$$HR2 = (S_{4.5-10.0} - S_{2.0-4.5}) / (S_{4.5-10.0} + S_{2.0-4.5}). \quad (5)$$

The hardness ratios, when applicable, can be found in Table 5. All measured hardness ratios (HR1) are positive, indicating that the LAE candidates are type 2 AGN (e.g. Norman et al. 2004). The low luminosity of the GALEX-detected candidates, assuming that they are [OII] emitters indicate that they are normal, star forming galaxies, or that they are Lyα emitters. The total sample of GALEX-detected and non-detected candidates without individual X-ray detections were stacked, and produced no detection in any band in a stack of 170 objects (the nine individual detections were removed from the stack, as well as eight candidates with unrelated objects detected in the vicinity). The non-detection in a stack of 170 objects imply an upper limit to the mean X-ray flux of approximately a factor of ten smaller than those in the catalogue of Cappelluti et al. (2007).

We also searched the catalogue of Schinnerer et al. (2007) for radio counterparts to the candidates. The data on which the catalogue is based was taken with the VLA array and covers the entire COSMOS field to a depth of a few $\times 10\mu$Jy. The catalogue presented in Schinnerer et al. (2007) contains 3643 source detections. This catalogue was searched with the same criteria as for the X-ray catalogue (i.e. detections within $8''$ of the candidate positions) and six objects were found. The number of random detections in a $8''$ radius aperture is 0.026. Of the six radio detections, one object is GALEX-detected (candidate 173). The radio fluxes of these sources can be found in Table 5. Only one source has a detection in both the X-ray and radio data. This is in principle not a problem since AGN can be both radio-loud and radio-quiet. The radio objects without X-ray detections are more enigmatic, but can be explained by the relatively shallow luminosity limit of the X-ray observations. If the radio fluxes are converted into star formation rates using the conversion rate of Condon (1992), they correspond to values in the range of $\sim 400 - \sim 1300\ M_\odot$ yr^{-1} whereas the upper limit to star formation rates in the XMM survey is $\sim 1200\ M_\odot$ yr^{-1}, using the conversion of Ranalli et al. (2003).

The AGN fraction of the non-GALEX-detected LAE sample is thus at least $\sim 5\%$, if it is assumed that the X-ray and radio objects within $5''$ of the narrow-band sources are true detections. It is clear that the shallow flux limit to the deepest X-ray band, corresponding to a luminosity of $\log(L_{0.5-2.0}) = 43.4$ erg s^{-1}, ensure many AGN of lower luminosities to be undetected, as confirmed by the radio detections without X-ray counterparts. The AGN fraction should therefore almost certainly be even higher, although we did not detect any X-ray flux in the mean, stacked total GALEX and non-GALEX-detected sample of 170 objects.

Previous studies of LAEs at higher redshifts exhibited very small AGN contributions, from less than one percent in the $z \sim 4.5$ LAEs studied by Wang et al. (2004) to ~1% at $z \sim 3$ as inferred by Gawiser et al. (2007). Lehmer et al. (2008) calculated the "AGN fraction function" of Lyα emitters at $z \sim 3$ both in the field and the overdense region of SSA22 (Fig. 3b in their paper). If we convert our 0.5−2.0 keV detection limit to their 8−32 keV luminosity range, we should expect to detect an AGN fraction of 0.5−1.5%, where the lower number is related to their field result and the higher to the SSA22 result. Based on this comprehensive study of X-ray detected Lyα emitting AGN, it is clear that the AGN fraction detected here is larger than at $z \sim 3$, as expected from the Lehmer et al. (2008) survey. Ouchi et al. (2008) argued that the missed fraction in AGN X-ray searches among LAEs may be as high as 10%. We performed the same test as in the Ouchi et al. (2008) publication. Based on the quasar SEDs of Elvis et al. (1994) and the UV spectrum of quasars of Telfer et al. (2002) and Richards et al. (2003) we inferred the ratio of observed 0.5−2.0 keV flux to Lyα flux of 1.87 and 1.51 for radio-quiet and radio-loud quasars, respectively . For the flux limit in the X-ray band, the maximum magnitude observed for Lyα is then 23.34. In our complete GALEX and non-GALEX-detected samples, nine objects have magnitudes brighter than this, four of which are GALEX-detected. Of the nine objects, six have X-ray detections (all four GALEX-detected sources and two LAE candidates). Thus, if we exclude the four GALEX-detected sources, two out of five Lyα bright galaxies host AGN and the fraction of X-ray detected AGN in the non-GALEX-detected sample is 40%, four times the fraction found by Ouchi et al. (2008) for $z \sim 3$ LAEs. To conclude, our detection of a 5% AGN contribution in the non-GALEX-detected LAE sample is consistent with previous results, but is indicative of a higher AGN fraction being present at this redshift.

4.3. Surface density, sizes and SFR

For the surface density determination, we included both the GALEX-detected and non-detected objects to obtain as complete as possible a measure of the number density. Since our image has areas of poorer signal-to-noise, as well as stellar artifacts, we selected sub-images of superior quality with a total area of ~288 arcmin^2, corresponding to ~28% of the total surveyed area, to use for the surface and volume density calculations. In these areas, the selection is complete, and we found 54 candidates within these sub-images. This implies a surface density of LAE candidates of 0.19 arcmin^{-2} Δz^{-1}, or 1.91 arcmin^{-2} z^{-1}. The volume density is 0.00062 Mpc^{-3}, which is in the lower range of that observed at redshift $z \sim 3$. Fynbo et al. (2001) summarise the surface densities of several early $z \sim 3$ surveys. With the exception of the Steidel et al. (2000) survey in the overdense SSA22 field, these surveys all determined values of 2.11−5.9 arcmin^{-2} z^{-1} to the flux limit of this survey, but with large error bars. Hence, the values at $z \gtrsim 3$ are consistently higher than our value, but in most cases the measurements agree to within 1σ. For LAE candidates brighter than the (5σ) luminosity limit of this survey, Nilsson et al. (2007) identified six candidates in their survey, corresponding to 0.0018 Mpc^{-3}, which represents a decrease of roughly a factor of three although based on a small sample. Gronwall et al. (2007) determined a space density of 0.00057 Mpc^{-3} above the 5σ luminosity limit of our survey, which is consistent with the space density found here. Stiavelli et al. (2001) presented a survey of $z = 2.4$ LAEs and found a volume density of 0.0001 Mpc^{-3} above a luminosity limit of $\log L = 42.93$ erg s^{-1}. The same number for this

survey is 0.00009 Mpc^{-3}. The numbers agree reasonably well with previous results. Finally, Prescott et al. (2008) completed a survey of $z \sim 2.7$ LAEs around a so-called Lyα blob (e.g. Steidel et al. 2000; Matsuda et al. 2004; Dey et al. 2005; Nilsson et al. 2006). They argued that the central part of their field is overdense, and determined a number density of 0.0021 Mpc^{-3}. This is roughly three and half times higher than in our survey. At the edge of their field, the density is instead 0.0012 Mpc^{-3}, in closer agreement with, but still higher than, our result. Thus, the surface density in this survey is in almost all cases lower than in higher redshift surveys, but could also be consistent with previous results. If one considers that number densities have been found to vary by factors of 2−5 in 0.2 deg^2 fields at redshift $z = 3$ (Ouchi et al. 2008), it is clear that more data at both higher and lower redshifts is needed to resolve this issue finally.

As in Nilsson et al. (2007), the sizes of the candidate Lyα and GALEX-detected objects measured in the narrow-band and r^+ broad-band images are presented in Fig. 7. Six LAE objects are excluded due to non-detections in the r^+ band. The *FWHM* was calculated using the FLUX_RADIUS output from SExtractor, and the PSF in the narrow-band image was calculated by using 9 objects in the image with fluxes in the range of the candidates and the SExtractor parameter CLASS_STAR larger than 0.8, which inferred a PSF of 0.96″. The PSF of the r^+ image is similar to that of the narrow-band image PSF (the PSF of the r^+ image is 1.06″). As can be seen in the figure, we have two marginal Lyα blob detections in this survey (of *FWHM* 3.46″ and 3.70″), if a Lyα blob is defined to have a radius larger than 15 kpc (corresponding to a diameter of 3.75″). These two (candidates 54 and 66) are also extended in the broadband images with *FWHM* $\sim 2''$ and are thus "normal" extended Lyα emitters. We conclude that we have no blobs in this survey. Using the results from Matsuda et al. (2004), Saito et al (2006), Gronwall et al. (2007), and Prescott et al. (2008), the expected number density of Lyman-alpha blobs ranges from a few to a few hundred $\times 10^{-6}$ Mpc^{-3}. The upper limit to the survey is ~3×10^{-6} Mpc^{-3}, and hence at the low end of the predictions from previous results. Matsuda et al. (2004) and Prescott et al. (2008) argued that Lyα blobs reside in overdense regions of space. If this assumption is correct, it agrees well with the two results from this survey that *i)* we detect a tentatively lower number density of LAEs at this redshift than expected from $z \sim 3$ observations, and *ii)* no Lyα blobs are found in this survey. Both these observations indicate that the COSMOS field is under-dense at $z = 2.25$. We also note that there is a rapid decline in *FWHM* at larger radii in Fig. 7, indicating that Lyα blobs and LAEs are two separate categories of Lyα emitting objects. If this was not the case, a tail of objects should be seen towards larger radii. No sample has yet been sufficiently large to confirm whether Lyα blobs and LAEs are separate populations. It is also apparent that the candidate emitters are in general always more extended in the narrow-band image than their broad-band counterparts, i.e. the broad-band counterparts are consistent with being pure point-sources whereas the narrow-band objects are significantly more extended than point-sources (cf. Møller & Warren 1998; Fynbo et al. 2001, 2003a). This may arise from diffuse scattering of Lyα within the galaxy (see also Laursen & Sommer-Larsen 2007) and/or due to the diffuse ISM (Östlin et al. 2008). The extent of this scattering is expected to be much smaller for [OII] emission, hence, the detection of significantly extended emission in a GALEX-detected object may therefore be indicative of it being a Lyα emitter.

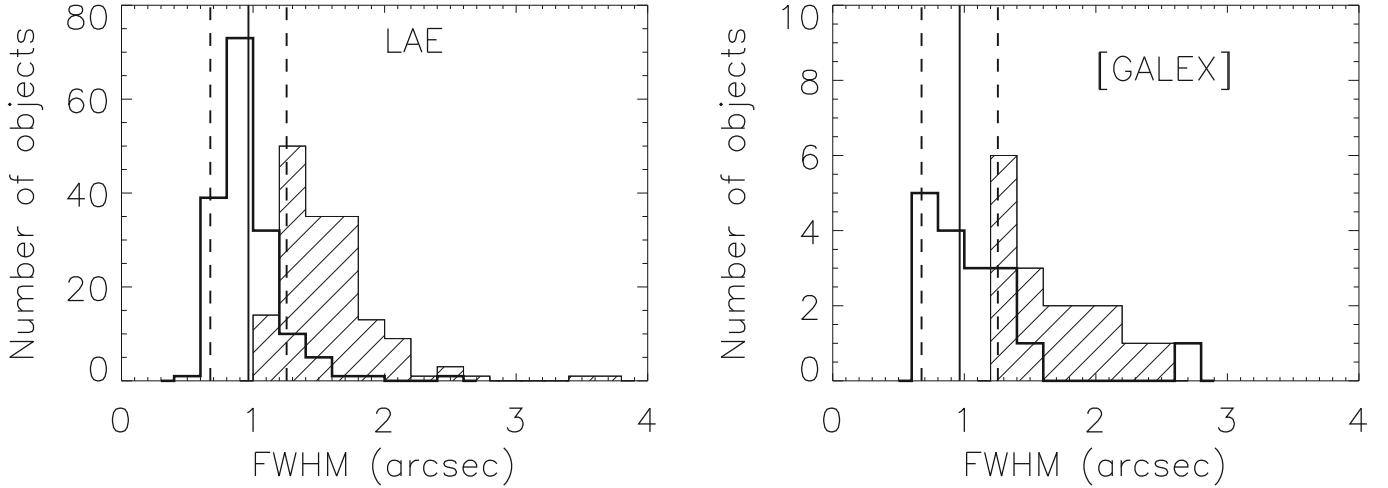The SFRs of the candidates are calculated using the common star formation indicators of the rest-frame UV continuum

Fig. 7. Size distribution of candidates as measured in the narrow-band (hatched histogram) and r^+ (empty histogram) images for LAE candidates and GALEX-detected candidates respectively. Sizes as measured by the FLUX_RADIUS command in SExtractor. The solid line represents the PSF of the narrow-band image, with the dotted lines showing the 1σ of the PSF measurement. These values are very similar to those of the r^+ image, see text.

emission at $\lambda = 1500$ Å and the Lyα emission. The Lyα emission used in this case was the continuum-subtracted narrow-band flux. The conversion rates that we use are the following:

$$SFR_{UV} = \frac{f_{1500\,Å} \times 4\pi d_L^2 \times 1.4 \times 10^{-28}}{1 + z} \, M_\odot \, \text{yr}^{-1} \quad (6)$$

where the flux density $f_{1500\,Å}$ is in erg s^{-1} cm^{-2} Hz^{-1}, d_L is the luminosity distance in centimeters and z the redshift (Kennicutt 1998). For Lyα, the conversion is:

$$SFR_{Ly\alpha} = \frac{F_{Ly\alpha} \times 4\pi d_L^2}{8.7 \times 1.12 \times 10^{41}} \, M_\odot \, \text{yr}^{-1} \quad (7)$$

where $F_{Ly\alpha}$ is the flux in the Lyα line in erg s^{-1} cm^{-2} (Brocklehurst 1971; Kennicutt 1983). A plot of the two resulting SFRs can be seen in Fig. 8. The SFRs are in the range of $\sim 1-30 \, M_\odot$ yr^{-1} in the Lyα measurement, some of which are unusually high for what is generally seen in Lyα emitters. The dashed line in Fig. 8 corresponds to a 1:1 relation between the UV/Lyα derived SFRs. A correlation is seen between the two measurements. The median of the ratio of UV-derived SFR to Lyα-derived SFR is 1.8. Looking at Eqs. (6) and (7), it is clear that a relation exists between the ratio of the two SFR measurements and the equivalent width of an object, such that:

$$\frac{SFR_{UV}}{SFR_{Ly\alpha}} \propto \frac{\text{const.}}{EW_0} . \quad (8)$$

In this equation, EW_0 is the rest-frame equivalent width of an object. The constant in the nominator depends on the spectral slope of the object, and on dust properties within the galaxy. For a flat slope in f_ν and no dust this constant equals 67 Å. For this assumption, our median ratio of 1.8 corresponds to a median EW of 37 Å, which is consistent with the measured median EW of 41.6 Å. The ratio is higher than that found by Ouchi et al. (2008), who measured a typical ratio of $\sim$1.2 in a sample of $z = 3.1$ LAEs, and Gronwall et al. (2007), who, after correcting for the $(1 + z)$ factor, also obtain a typical ratio of $\sim$1.0 (Gronwall, priv. communication). These results are also related to those presented in Sect. 4.4. We note that several objects have ratios of below one. In total, 19 objects have measurements that deviate by up to 3σ from the 1:1 line. The explanation for these
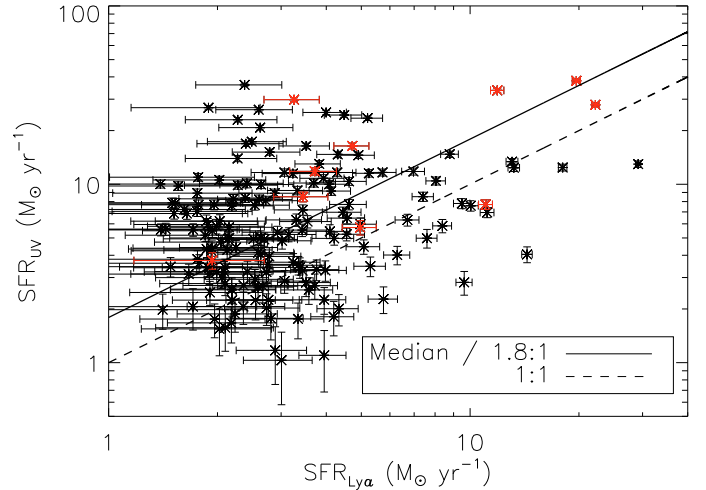

Fig. 8. Star formation rates as derived from the UV rest-frame 1500 Å emission and the Lyα emission for the sample of the 170 candidates. Red points indicate the AGN in the sample, plotted for reference. The measurements correlate well. The solid line indicates the median of the fraction of SFR from the UV and Lyα in the sample, and the dashed line indicates a 1:1 ratio between the two measurements.

measurements may originate in the age dependence of the UV SFR conversion factor. According to Kennicutt et al. (1998), the constant in Eq. (6) is valid for galaxies with constant star formation in the past $\geq 10^8$ yrs. For starbursts of younger ages, the conversion factor should increase. This would bring the ratios closer to the 1:1 line. It appears true for at least 11% of the sample (19 out of 170), which show signs of young starburst activity.

4.4. Equivalent width distribution

At higher redshift ($z \gtrsim 4$), emitters with EWs larger than 240 Å have been predicted (Schaerer 2003; Tumlison et al. 2003) and observed (Malhotra & Rhoads 2002; Shimasaku et al. 2006; Stanway et al. 2007). These large EWs supposedly cannot be explained by a normal initial mass function but have been proposed to be signs of Population III stars. At redshift $z \sim 3$, small subsamples of detected emitters exhibit extremely high EWs (a few
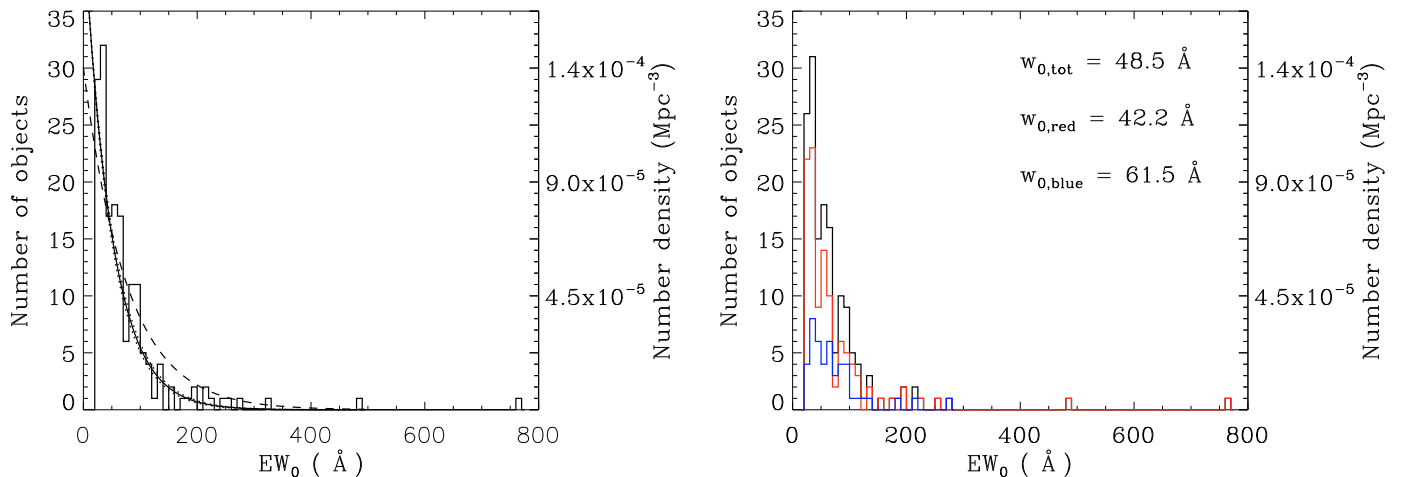
Fig. 9. *Left*: distribution of restframe equivalent widths of the sample of 170 candidates. Bin size is 10 Å. The solid line indicates the exponential fit to the data with the fits with $\pm 1\sigma$ plotted with dotted lines. The dashed line is the best fit to the sample of Gronwall et al. (2007). This sample has a more narrow distribution of equivalent widths. *Right*: distribution of restframe equivalent widths for total (non-GALEX-detected), red and blue sample (with $Vj-^+ >$ or < 0). In this plot, only objects with detections in both the Vj and the i^+ bands are given. Red sample is plotted with a red line and blue with a blue line. The width of the different distributions are given in the figure.

percent in the surveys of both Gronwall et al. 2007; and Nilsson et al. 2007; and up to 20% in Ouchi et al. 2008). In Fig. 9, the distribution of rest-frame equivalent widths of the candidates can be seen, also divided into the red and blue sub-samples. The sample includes six emitters with restframe *EW*s larger than 240 Å, corresponding to ~4%.

In Gronwall et al. (2007), the data is reproduced with an exponentially declining function:

$$N = C \times e^{-EW/w_0} \qquad (9)$$

where N is the number of objects, C is a normalisation constant and w_0 is the e-folding length of the distribution. Gronwall et al. (2007) inferred that $w_0 = 76^{+11}_{-8}$ Å. The *EW* distribution presented here was fitted here by a best-fit solution minimising the χ^2, and the errors of the fit were calculated by producing 100 000 distributions, normally distributed within the margins of errors in the equivalent widths. Each cumulative distribution was reproduced by an exponential function. No correction for filter transmission curve was done since the filter is nearly box-shaped (see also Fig. 1). The best-fit solution to the e-folding *EW* for the total non-GALEX-detected sample is $w_{0,tot} = 48.5 \pm 1.7$ Å, less than two thirds of that inferred by Gronwall et al. (2007). This implies that, at $z = 2.25$, there is a higher fraction of LAEs with small *EW*s than at $z = 3.1$. Corresponding values for the red and blue sub-samples are $w_{0,red} = 42.2 \pm 1.7$ and $w_{0,blue} = 61.5 \pm 4.5$, respectively. The fits indicate that the redder galaxies have a narrower distribution than the bluer galaxies, a result also consistent with the redder galaxies being dustier than the bluer galaxies. This relation was previously observed for LBGs (Shapley et al. 2003).

Since the Lyα *EW* of a starburst declines with time (Charlot & Fall 1993; Schaerer 2003) one might seek to interpret the change in width of the distributions in the redshift interval $z = 3-2$ as a simple evolution of individual objects. To test this simple idea, we attempted to recreate both the $z = 3.1$ and $z = 2.25$ *EW* distribution from the simple evolution of single stellar population starbursts by using both the predictions of Charlot & Fall (1993) and Schaerer (2003). We found that neither of the two distributions can be recreated in this way. The decline in the

Lyα *EW* of a starburst is so rapid that a cumulative *EW* distribution similar to those in Fig. 9 will be much narrower than those observed at both redshifts. The only way of obtaining distributions similar to those observed is to allow the majority of the galaxies to have continuous star formation. We can therefore conclude that at maximum a small fraction of the LAEs at redshifts $z = 2-3$ are single starburst objects, and are most likely better explained by alternative star formation histories. Finally, the shift in the width of the distribution between $z = 3$ and $z = 2$ cannot be explained by simple evolution with time, but is further evidence of a higher dust content in LAEs at redshift $z \sim 2$. Worth noting is that a narrower *EW* distribution is consistent with the higher UV-to-Lyα SFRs described in Sect. 4.3 since the *EW* is proportional to the ratio of the flux in the Lyα to the flux density in the UV, similar to the SFRs.

5. Conclusion

In this paper, the observations and selection leading to a sample of 170 robust LAE candidates at $z = 2.25$ have been presented. This is the first large-scale survey of LAEs at redshifts around two, and several indications of evolution are seen in the properties of LAEs between redshift $z \sim 3$ and $z \sim 2$. This is however unsurprising, since the separation in these redshifts corresponds to longer than 1 Gyr. The main arguments for an evolution in the properties of this type of galaxy are:

– *The large spread in SEDs*

The most conspicuous evolution detected was that of the emergence of a large number of "red" LAEs. The 12 individual detections in the relatively shallow K_s images and the red mean SED of the total stacked sample, presented in Fig. 6, indicated that a significant subsample, of up to two-thirds of the total sample, of LAEs are massive, and potentially dusty, galaxies. We also showed that the rest-frame UV colours of these galaxies cannot be explained by a simple stellar population, and that even though the majority of the candidates are consistent with being young galaxies, a significant fraction of the sample displays more complicated colours.

– *Potentially larger fraction of AGN*

The result above is also related to the detection of at least nine AGN in the sample. Again, this is not a surprising result since redshift $z \sim 2$ corresponds to the peak of the AGN number density distribution (see e.g. Wolf et al. 2003, and references therein). The number density of AGN in this sample is in principle consistent with surveys at higher redshift, but is likely to be higher by a factor of two.

– *Change in SFR ratios*

The ratio of UV to Lyα derived SFRs has a higher median value in this survey than results at redshift $z \sim 3$. The spread is large, but the trend is clear. This result, and the smaller *EW*s discovered in general for this sample (see also the next point) at high redshift may indicate that LAEs in this survey are expected to be more affected by dust than LAEs at $z \sim 3$.

– *Narrower EW distribution*

Another intriguing and related result is that of the narrower equivalent width distribution. Firstly, as detailed in Sect. 4.4, the distribution is difficult to explain without invoking complicated arguments about the properties of the galaxies. A possible explanation would be that the star formation histories of Lyα emitters are complex. Secondly, the difference in the distributions between redshifts three and two is further evidence of a higher dust quantity in the lower redshift galaxies.

In conclusion, by comparing observations of Lyα emitters at redshift $z = 2.25$ with galaxies selected in the same manner at higher redshifts, several evolutionary signatures become evident in the properties of these galaxies. At lower redshifts, there appear to be fewer objects, with redder colours and higher dust contents, smaller equivalent widths, and a higher fraction of objects containing AGN. Future SED fitting of these galaxies will reveal more information into the properties such as dust, mass and age (Nilsson et al., in prep.).

References

Baade, D., Meisenheimer, K., & Iwert, O., et al. 1999, The Messenger, 95, 15
Bertin, E., & Arnouts, S. 1996, A&AS, 117, 393
Bongiorno, A., Zamorani, G., & Gavignaud, I., et al. 2007, A&A, 472, 443
Brocklehurst, M. 1971, MNRAS, 153, 471
Bruzual, G. A., & Charlot, S. 2003, MNRAS, 344, 1000
Calzetti, D. 2001, PASP, 113, 1449
Calzetti, D., Armus, L., & Bohlin, R. C., et al. 2000, ApJ, 533, 682
Capak, P., Aussel, H., & Ajiki, M., et al. 2007, ApJS, 172, 99
Cappelluti, N., Hasinger, G., & Brusa, M., et al. 2007, ApJS, 172, 341
Charlot, S., & Fall, S. M. 1993, ApJ, 415, 580
Condon, J. J. 1992, ARA&A, 30, 575
Cowie, L. L., & Hu, E. M. 1998, AJ, 115, 1319
Dey, A., Bian, C., Soifer, B. T., et al. 2005, ApJ, 629, 654
Elvis, M., Wilkes, B. J., & McDowell, J. C., et al. 1994, ApJS, 95, 1
Finkelstein, S. L., Rhoads, J. E., Malhotra, S., Pirzkal, N., & Wang, J. 2007, ApJ, 660, 1023
Finkelstein, S. L., Rhoads, J. E., Malhotra, S., & Grogin, N. 2009, ApJ, 691, 465

Francis, P. J., Palunas, P., Teplitz, H. I., Williger, G. M., & Woodgate, B. E. 2004, ApJ, 614, 75
Freedman, W. L., Madore, B. F., & Gibson, B. K., et al. 2001, ApJ, 553, 47
Fynbo, J. U., Møller, P., & Warren, S. J. 1999, MNRAS, 305, 849
Fynbo, J. P. U., Møller, P., & Thomsen, B. 2001, A&A, 374, 443
Fynbo, J. P. U., Møller, P., & Thomsen, B., et al. 2002, A&A, 388, 425
Fynbo, J. P. U., Ledoux, C., Møller, P., Thomsen, B., & Burud, I. 2003a, A&A, 407, 147
Fynbo, J. P. U., Jakobsson, P., & Möller, P., et al. 2003b, A&A, 406, L63
Gabasch, A., Goranova, Y., Hopp, U., Noll, S., & Pannella, M. 2008, MNRAS, 383, 1319
Gallego, J., García-Dabó, C., Zamorano, J., Aragón-Salamanca, A., & Rego, M. 2002, ApJ, 570, L1
Gawiser, E., Van Dokkum, P. G., & Gronwall, C., et al. 2006, ApJ, 642, L13
Gawiser, E., Francke, H., & Lai, K., et al. 2007, ApJ, 671, 278
Gronwall, C., Ciardullo, R., & Hickey, T., et al. 2007, ApJ, 667, 79
Hasinger, G., Cappelluti, N., & Brunner, H., et al. 2007, ApJS, 172, 29
Hathi, N. P., Malhotra, S., & Rhoads, J. E. 2008, ApJ, 673, 686
Hayes, M., & Östlin, G. 2006, A&A, 460, 681
Hayes, M., Östlin, G., Mas-Hesse, J. M., & Kunth, D. 2008, AJ, submitted, [arXiv:0803.1176]
Hogg, D. W., Cohen, J. G., Blandford, R., & Pahre, M. A. 1998, ApJ, 504, 622
Kashikawa, N., Shimasaku, K., & Malkan, M. A., et al. 2006, ApJ, 648, 7
Kennicutt, R. C. 1983, ApJ, 272, 54
Kennicutt, R. C. 1998, ARA&A, 36, 189
Kewley, L. J., Geller, M. J., & Jansen, R. A. 2004, AJ, 127, 2002
Lai, K., Huang, J.-S., & Fazio, G., et al. 2008, ApJ, 674, 70
Laursen, P., & Sommer-Larsen, J. 2007, ApJ, 567, L69
Lehmer, B. D., Alexander, D. M., & Geach, J. E., et al. 2008, ApJ, 691, 687
Ly, C., Malkan, M. A., Kashikawa, N., et al. 2007, ApJ, 657, 738
Malhotra, S., & Rhoads, J. E. 2002, ApJ, 565, L71
Malhotra, S., Rhoads, J. E., & Pirzkal, N., et al. 2005, ApJ, 626, 666
Matsuda Y., Yamada T., & Hayashino T., et al. 2004, AJ, 128, 569
Matsuda, Y., Yamada, T., & Hayashino, T., et al. 2005, ApJ, 634, L125
Meurer, G. R., Heckman, T. M., Lehnert, M. D., Leitherer, C., & Lowenthal, J. 1997, AJ, 114, 54
Møller, P., & Jakobsen, P. 1990, A&A, 228, 299
Møller, P., & Warren, S. J. 1993, A&A, 270, 43
Møller, P., & Warren, S. J. 1998, MNRAS, 299, 661
Nilsson, K. K., Fynbo, J. P. U., Møller, P. S., Larsen, J., & Ledoux, C. 2006, A&A, 452, L23
Nilsson, K. K., Møller, P., & Möller, O., et al. 2007, A&A, 471, 71
Norman, C., Ptak, A., Hornschemeier, A., et al. 2004, ApJ, 607, 721
Ouchi, M., Shimasaku, K., Akiyama, M., et al. 2008, ApJS, 176, 301
Pentericci, L., Kurk, J. D., Röttgering, H. J. A., et al. 2000, A&A, 361, L25
Pirzkal, N., Malhotra, S., Rhoads, J. E., & Xu, C. 2007, ApJ, 667, 49
Prescott, M. K. M., Kashikawa, N., Dey, A., & Matsuda, Y. 2008, ApJ, 678, L77
Ranalli, P., Comastri, A., & Setti, G. 2003, A&A, 399, 39
Richards, G. T., Hall, P. B., & Vanden Berk, D. E., et al. 2003, AJ, 126, 1131
Saito, T., Shimasaku, K., & Okamura, S., et al. 2006, ApJ, 648, 54
Schaerer, D. 2003, A&A, 397, 527
Shapley, A. E., Steidel, C. C., Pettini, M., & Adelberger, K. L. 2003, ApJ, 588, 65
Shimasaku, K., Kashikawa, N., & Doi, M., et al. 2006, PASJ, 58, 313
Shinnerer, E., Smolcić, V., & Carilli, C. L., et al. 2007, ApJS, 172, 46
Siana, B., Teplitz, H. I., & Colbert, J., et al. 2007, ApJ, 668, 62
Stanway, E. R., Bunker, A. J., & Glazebrook, K., et al. 2007, MNRAS, 376, 727
Stiavelli, M., Scarlata, C., & Panagia, N., et al. 2001, ApJ, 561, L37
Steidel, C. C., Adelberger, K., & Shapley, A. E., et al. 2000, ApJ, 532, 170
Taniguchi, Y., Ajiki, M., & Nagao, T., et al. 2005, PASJ, 57, 165
Tapken, C., Appenzeller, I., & Gabasch, A., et al. 2006, A&A, 455, 145
Telfer, R. C., Zheng, W., Kriss, G. A., & Davidsen, A. F. 2002, ApJ, 565, 773
Teplitz, H. I., Collins, N. R., Gardner, J. P., Hill, R. S., & Rhodes, J. 2003, ApJ, 589, 704
Tumlinson, J., Shull, J. M., & Venkatesan, A. 2003, ApJ, 584, 608
Van Breukelen, C., Jarvis, M. J., & Venemans, B. P. 2005, MNRAS, 359, 895
Venemans, B. P., Röttgering, H. J. A., Miley, G. K., et al. 2007, A&A, 461, 823
Wang, J. X., Rhoads, J. E., Malhotra, S., et al. 2004, ApJ, 608, L21
Wolf, C., Wisotzki, L., Borch, A., et al. 2003, A&A, 408, 499
Östlin, G., Hayes, M., & Kunth, D., et al. 2008, AJ, submitted, [arXiv:0803.1174]

Table 2. Coordinates, observed equivalent widths, continuum subtracted narrow-band magnitudes and UV spectral index β of the candidates.

LAE_COSMOS_#	R.A.	Dec.	EW (Å)	Mag$_{3960}$	β	
			Rank 1 candidates			
1	150.05310	1.94797	142.7 ± 38.6	25.50 ± 0.34	−0.48 ± 0.24	
2	150.21068	1.95100	225.8 ± 57.0	25.41 ± 0.32	−0.82 ± 0.33	
3	150.29437	1.95107	564.0 ± 43.2	24.24 ± 0.09	−1.40 ± 0.40	
4	150.25458	1.95224	118.4 ± 33.4	25.55 ± 0.36	−2.12 ± 0.33	
5	150.31830	1.95244	279.3 ± 41.8	24.91 ± 0.18	−2.08 ± 0.44	
6	150.37505	1.95619	95.9 ± 24.2	25.46 ± 0.32	−1.84 ± 0.29	
7	150.15936	1.95717	790.3 ± 140.1	25.04 ± 0.21	−2.97 ± 1.06	
8	150.37990	1.96143	119.6 ± 16.8	24.88 ± 0.16	1.81 ± 0.22	G
9	150.28378	1.96167	248.1 ± 50.2	25.20 ± 0.25	−1.84 ± 0.34	
10	150.30785	1.96243	81.0 ± 28.5	25.79 ± 0.47	0.54 ± 0.26	
11	150.09872	1.96394	112.8 ± 18.1	25.02 ± 0.19	0.78 ± 0.23	G
12	150.34027	1.96410	81.7 ± 18.2	25.36 ± 0.27	−1.43 ± 0.24	G
13	150.02708	1.96733	516.5 ± 49.7	24.47 ± 0.11	−1.23 ± 0.33	
14	149.99709	1.96769	112.8 ± 17.0	24.96 ± 0.18	0.30 ± 0.19	
15	150.08733	1.96782	119.0 ± 26.6	25.34 ± 0.28	0.35 ± 0.23	
16	150.20992	1.97043	430.0 ± 18.0	23.61 ± 0.05	−2.15 ± 0.23	
17	149.94597	1.97057	125.3 ± 31.6	25.44 ± 0.32	−1.53 ± 0.32	G
18	150.08206	1.97149	225.1 ± 30.1	24.81 ± 0.16	2.19 ± 0.27	G
19	149.94090	1.97264	94.0 ± 26.0	25.56 ± 0.35	−1.11 ± 0.29	
20	150.11101	1.97300	728.8 ± 12.2	22.57 ± 0.02	−1.62 ± 0.16	
21	150.37648	1.97352	375.0 ± 79.2	25.22 ± 0.26	−2.24 ± 0.68	
22	149.86295	1.97367	91.0 ± 24.9	25.55 ± 0.35	−1.58 ± 0.28	
23	150.15871	1.97373	257.9 ± 43.0	25.02 ± 0.20	−1.84 ± 0.50	
24	150.13911	1.97409	193.8 ± 38.5	25.20 ± 0.24	−1.06 ± 0.41	G
25	150.10304	1.97874	196.4 ± 55.4	25.52 ± 0.36	−1.15 ± 0.40	
26	149.96286	1.97933	140.6 ± 20.0	24.89 ± 0.17	−1.95 ± 0.24	
27	150.06393	1.98022	205.5 ± 7.5	23.44 ± 0.04	−2.39 ± 0.15	
28	149.89557	1.98102	161.5 ± 29.4	25.12 ± 0.22	−2.11 ± 0.38	
29	150.06519	1.98162	187.0 ± 53.4	25.53 ± 0.37	−1.20 ± 0.49	
30	150.17101	1.98264	103.5 ± 10.0	24.51 ± 0.11	−1.68 ± 0.15	
31	150.18777	1.98536	307.0 ± 77.0	25.38 ± 0.31	−2.86 ± 0.60	
32	150.24959	1.98880	1049.2 ± 136.0	24.74 ± 0.15	−2.36 ± 1.09	
33	150.24374	1.99106	606.4 ± 77.8	24.74 ± 0.15	−2.86 ± 0.54	
34	150.37790	1.99192	195.2 ± 32.7	25.03 ± 0.20	−1.80 ± 0.34	
35	150.06696	1.99623	91.5 ± 27.0	25.62 ± 0.38	−0.44 ± 0.25	
36	150.23073	1.99868	237.8 ± 5.3	22.87 ± 0.02	−1.36 ± 0.11	
37	150.16040	2.00118	266.1 ± 31.0	24.67 ± 0.13	−1.10 ± 0.30	
38	150.30551	2.00346	94.0 ± 32.9	25.77 ± 0.47	−0.21 ± 0.26	
39	150.03159	2.00354	285.5 ± 17.7	24.03 ± 0.07	−2.38 ± 0.38	
40	149.94576	2.00370	111.5 ± 22.0	25.22 ± 0.24	−1.22 ± 0.24	
41	150.36711	2.00375	119.6 ± 28.6	25.40 ± 0.30	−1.69 ± 0.30	
42	149.99530	2.00661	127.4 ± 3.0	22.87 ± 0.03	−0.12 ± 0.07	G
43	149.85944	2.01134	194.1 ± 31.0	24.99 ± 0.19	−1.75 ± 0.34	
44	150.15681	2.01215	90.6 ± 35.3	25.87 ± 0.54	1.49 ± 0.22	
45	150.02440	2.01287	265.8 ± 79.8	25.55 ± 0.39	−1.74 ± 0.43	
46	150.14574	2.02141	111.7 ± 23.6	25.29 ± 0.26	−0.88 ± 0.22	
47	150.20502	2.02257	709.1 ± 23.0	23.34 ± 0.04	−2.93 ± 0.33	
48	150.27144	2.02501	127.5 ± 30.6	25.40 ± 0.30	−1.31 ± 0.30	
49	150.28159	2.02530	96.0 ± 21.2	25.34 ± 0.27	0.57 ± 0.14	
50	149.92310	2.02684	122.9 ± 6.1	23.77 ± 0.05	−0.82 ± 0.09	G
51	150.33127	2.03051	105.6 ± 24.5	25.38 ± 0.29	−0.33 ± 0.26	
52	150.18434	2.03525	188.0 ± 22.5	24.71 ± 0.14	−0.13 ± 0.20	
53	150.13292	2.03638	156.8 ± 40.2	25.45 ± 0.32	−1.28 ± 0.44	
54	149.88849	2.04398	129.3 ± 36.2	25.54 ± 0.36	4.31 ± 0.18	
55	150.16479	2.04481	692.3 ± 149.9	25.22 ± 0.27	0.76 ± 0.52	
56	150.37027	2.04687	171.0 ± 42.6	25.41 ± 0.31	−1.11 ± 0.41	
57	149.93562	2.04905	139.7 ± 20.6	24.93 ± 0.17	−1.26 ± 0.21	
58	150.13397	2.05000	185.2 ± 47.1	25.43 ± 0.32	−2.19 ± 0.46	
59	149.93231	2.05110	221.6 ± 69.9	25.61 ± 0.41	−1.54 ± 0.44	
60	150.35435	2.05145	201.0 ± 56.9	25.52 ± 0.36	−1.28 ± 0.36	
61	150.28970	2.05283	91.1 ± 24.1	25.52 ± 0.33	−1.94 ± 0.29	
62	150.23158	2.05635	94.9 ± 33.5	25.78 ± 0.47	0.10 ± 0.28	
63	149.92773	2.06066	87.0 ± 15.2	25.12 ± 0.21	0.05 ± 0.16	
64	150.06021	2.06279	95.2 ± 19.7	25.28 ± 0.25	−0.86 ± 0.22	
65	150.20416	2.06312	179.1 ± 48.3	25.48 ± 0.34	−0.50 ± 0.45	
66	150.14621	2.06399	81.8 ± 16.1	25.24 ± 0.24	1.69 ± 0.17	
67	149.96448	2.06816	224.8 ± 21.7	24.49 ± 0.11	−1.58 ± 0.29	

Table 2. continued.

			Rank 1 candidates			
LAE_COSMOS_#	R.A.	Dec.	*EW* (Å)	Mag$_{3960}$	β	
68	149.91591	2.06853	203.3 ± 49.5	25.38 ± 0.30	−1.17 ± 0.53	
69	149.90701	2.06886	328.7 ± 46.3	24.85 ± 0.16	−2.40 ± 0.49	
70	150.02284	2.06921	181.4 ± 43.6	25.38 ± 0.30	−2.65 ± 0.56	
71	150.06326	2.07060	213.7 ± 25.5	24.70 ± 0.14	−2.01 ± 0.30	
72	150.27551	2.07638	107.4 ± 39.4	25.80 ± 0.50	−2.24 ± 0.40	
73	149.84912	2.07790	208.5 ± 22.7	24.61 ± 0.13	−1.96 ± 0.25	
74	150.06166	2.08543	167.3 ± 32.3	25.18 ± 0.23	−1.86 ± 0.43	
75	149.89363	2.08908	87.7 ± 19.9	25.37 ± 0.28	−1.28 ± 0.22	
76	149.89395	2.09089	107.9 ± 12.5	24.69 ± 0.13	−2.05 ± 0.20	
77	150.30180	2.09191	276.5 ± 52.7	25.14 ± 0.23	−2.11 ± 0.63	
78	149.97191	2.09257	124.2 ± 11.2	24.43 ± 0.10	−1.67 ± 0.17	
79	150.07747	2.09275	181.9 ± 75.6	25.86 ± 0.58	−3.10 ± 0.61	
80	149.88147	2.09729	102.0 ± 19.1	25.18 ± 0.23	−0.48 ± 0.21	
81	149.94656	2.09879	114.7 ± 29.4	25.47 ± 0.32	−0.01 ± 0.21	
82	150.06995	2.10158	100.1 ± 4.1	23.54 ± 0.05	−1.36 ± 0.10	
83	149.99304	2.10211	198.6 ± 20.7	24.57 ± 0.12	−0.97 ± 0.26	
84	149.87749	2.10238	111.8 ± 18.8	25.06 ± 0.20	−1.64 ± 0.28	
85	150.21191	2.10867	256.3 ± 51.8	25.20 ± 0.25	−2.56 ± 0.52	
86	150.15732	2.11602	236.9 ± 79.0	25.65 ± 0.44	−3.11 ± 0.89	
87	150.08798	2.11824	186.3 ± 10.9	23.97 ± 0.07	−2.15 ± 0.18	
88	149.90225	2.11884	181.1 ± 42.7	25.36 ± 0.29	−3.28 ± 0.59	
89	150.33504	2.12015	88.6 ± 26.1	25.62 ± 0.38	−0.86 ± 0.22	
90	149.99657	2.12323	229.3 ± 73.6	25.62 ± 0.42	−0.91 ± 0.43	
91	149.94440	2.12351	317.9 ± 83.8	25.43 ± 0.33	−1.69 ± 0.75	
92	150.33075	2.12582	386.2 ± 10.2	23.09 ± 0.03	−2.18 ± 0.16	
93	150.35118	2.12592	165.0 ± 38.3	25.35 ± 0.29	−1.64 ± 0.34	
94	149.86707	2.12940	2494.5 ± 212.8	24.33 ± 0.10	−0.51 ± 0.61	
95	149.90939	2.13208	618.8 ± 74.2	24.68 ± 0.14	−2.78 ± 0.68	
96	149.84438	2.13389	90.9 ± 17.2	25.19 ± 0.23	−1.53 ± 0.22	
97	150.24510	2.13715	433.2 ± 122.0	25.47 ± 0.36	−0.25 ± 0.99	
98	150.29857	2.14162	90.3 ± 33.8	25.84 ± 0.51	−1.08 ± 0.29	
99	149.97021	2.14380	282.2 ± 40.3	24.87 ± 0.17	−2.27 ± 0.51	
100	150.28624	2.14409	176.5 ± 25.5	24.89 ± 0.17	−1.48 ± 0.29	
101	150.23888	2.14416	303.5 ± 29.6	24.49 ± 0.11	−1.37 ± 0.31	
102	150.31487	2.15756	151.3 ± 46.4	25.61 ± 0.40	−0.17 ± 0.26	
103	150.34485	2.15873	306.9 ± 46.6	24.92 ± 0.18	−2.20 ± 0.39	
104	150.24129	2.16620	121.7 ± 32.0	25.49 ± 0.33	−1.04 ± 0.32	
105	150.28941	2.16687	113.8 ± 39.7	25.75 ± 0.47	−1.26 ± 0.20	
106	150.26569	2.17274	206.7 ± 21.9	24.58 ± 0.12	−1.77 ± 0.26	
107	150.23207	2.17309	266.1 ± 38.9	24.89 ± 0.17	−2.53 ± 0.43	
108	149.89485	2.17439	129.6 ± 3.7	23.12 ± 0.03	0.35 ± 0.08	G
109	150.29601	2.17828	124.3 ± 24.9	25.23 ± 0.24	−2.19 ± 0.31	
110	150.03015	2.18227	214.7 ± 61.4	25.52 ± 0.37	−0.76 ± 0.41	
111	150.05544	2.18266	205.9 ± 44.5	25.27 ± 0.26	−2.11 ± 0.46	
112	149.88132	2.18599	106.1 ± 14.6	24.87 ± 0.16	−0.47 ± 0.16	
113	150.06270	2.18875	165.9 ± 8.9	23.87 ± 0.06	−1.62 ± 0.15	
114	149.87740	2.19040	174.7 ± 48.0	25.50 ± 0.35	−2.71 ± 0.56	
115	150.37823	2.19638	161.9 ± 4.1	23.00 ± 0.03	−1.06 ± 0.09	
116	150.19789	2.19923	334.7 ± 30.4	24.42 ± 0.10	−2.22 ± 0.40	
117	150.34007	2.20841	94.3 ± 20.8	25.34 ± 0.27	−0.06 ± 0.18	
118	149.87099	2.21710	138.6 ± 11.5	24.34 ± 0.09	−1.75 ± 0.17	
119	150.19261	2.21984	94.5 ± 14.0	24.95 ± 0.17	0.64 ± 0.12	
120	150.14146	2.22108	175.0 ± 11.1	24.06 ± 0.07	−2.49 ± 0.20	
121	150.34402	2.22653	117.2 ± 21.5	25.15 ± 0.22	−1.47 ± 0.22	
122	150.18269	2.22997	220.5 ± 75.6	25.68 ± 0.46	0.17 ± 0.51	
123	149.87993	2.23833	121.7 ± 34.7	25.56 ± 0.36	0.36 ± 0.36	
124	150.05911	2.24064	305.5 ± 10.9	23.43 ± 0.04	−1.76 ± 0.18	
125	149.90793	2.24599	82.4 ± 26.5	25.71 ± 0.42	−0.44 ± 0.24	
126	150.34988	2.24613	123.4 ± 2.9	22.88 ± 0.03	−0.13 ± 0.06	G
127	150.35498	2.24640	116.4 ± 24.6	25.28 ± 0.26	−0.04 ± 0.16	
128	150.14888	2.25189	425.8 ± 81.6	25.13 ± 0.23	—	
129	150.26230	2.25639	93.2 ± 12.0	24.81 ± 0.15	−0.49 ± 0.20	
130	149.84639	2.25665	393.7 ± 73.5	25.10 ± 0.22	−0.10 ± 0.40	G
131	150.22411	2.25913	139.8 ± 20.8	24.93 ± 0.17	−1.90 ± 0.27	
132	150.01633	2.26099	144.8 ± 27.7	25.18 ± 0.23	−1.73 ± 0.32	
133	150.20218	2.27326	268.5 ± 70.7	25.43 ± 0.33	−1.30 ± 0.46	

[a] Coordinates are in J2000. Candidates marked with the capital letter G are detected with GALEX, see text below.

Table 2. continued.

LAE_COSMOS_#	R.A.	Dec.	EW (Å)	Mag$_{3960}$	β	
			Rank 1 candidates			
134	149.85149	2.27637	97.9 ± 20.6	25.29 ± 0.26	2.31 ± 0.13	
135	150.28336	2.29025	194.0 ± 36.9	25.16 ± 0.23	−0.92 ± 0.34	
136	150.11346	2.29208	301.9 ± 21.3	24.17 ± 0.08	−1.62 ± 0.27	
137	149.84589	2.29449	134.9 ± 34.6	25.46 ± 0.32	−1.39 ± 0.33	
138	149.92577	2.29649	392.3 ± 90.8	25.30 ± 0.29	−1.69 ± 0.61	
139	149.91452	2.29848	89.4 ± 15.1	25.08 ± 0.20	−1.76 ± 0.20	
140	150.13303	2.30323	83.8 ± 8.4	24.55 ± 0.11	−1.23 ± 0.15	
141	150.38214	2.30512	88.6 ± 26.9	25.65 ± 0.39	−1.82 ± 0.28	
142	149.88753	2.31025	170.9 ± 11.6	24.12 ± 0.08	−1.81 ± 0.17	
143	150.28444	2.31210	122.2 ± 33.8	25.54 ± 0.35	−2.30 ± 0.40	
144	150.18822	2.31425	1560.5 ± 378.7	25.30 ± 0.30	2.24 ± 0.96	
145	150.19975	2.31548	123.1 ± 37.1	25.61 ± 0.39	0.62 ± 0.22	
146	149.84724	2.31988	296.8 ± 46.6	24.96 ± 0.19	−1.28 ± 0.46	
147	150.35138	2.32247	121.7 ± 23.5	25.19 ± 0.23	1.08 ± 0.14	
148	150.34016	2.32426	119.0 ± 14.6	24.75 ± 0.14	−1.56 ± 0.18	
149	149.84915	2.32473	319.7 ± 61.1	25.13 ± 0.23	−2.01 ± 0.44	
150	150.16183	2.33232	277.0 ± 40.4	24.89 ± 0.17	1.42 ± 0.28	
151	150.01070	2.33294	227.5 ± 31.9	24.86 ± 0.16	−0.49 ± 0.28	
152	149.86371	2.33722	141.4 ± 12.9	24.44 ± 0.10	1.30 ± 0.14	
153	149.87315	2.33814	294.5 ± 56.6	25.14 ± 0.23	−2.22 ± 0.42	
154	149.93753	2.34187	327.5 ± 44.2	24.81 ± 0.16	−2.38 ± 0.48	
155	149.87184	2.34282	102.1 ± 2.0	22.60 ± 0.02	−1.58 ± 0.06	G
156	149.95053	2.34326	135.1 ± 16.3	24.73 ± 0.14	2.83 ± 0.16	
157	149.88994	2.34619	100.8 ± 12.6	24.77 ± 0.14	−1.31 ± 0.18	G
158	150.28763	2.35091	137.6 ± 34.2	25.43 ± 0.31	−2.08 ± 0.39	
159	150.20575	2.35936	265.2 ± 35.0	24.79 ± 0.15	−2.68 ± 0.42	
160	150.27786	2.36288	304.4 ± 56.6	25.11 ± 0.22	−3.04 ± 0.70	
161	150.34100	2.36718	492.4 ± 20.9	23.63 ± 0.05	−0.29 ± 0.24	
162	150.02017	2.37396	224.6 ± 55.0	25.38 ± 0.30	−1.75 ± 0.51	
163	150.26894	2.37526	381.2 ± 76.2	25.17 ± 0.24	−1.44 ± 0.61	
164	150.10027	2.37696	147.6 ± 15.3	24.57 ± 0.12	−1.31 ± 0.19	
165	150.30130	2.37698	603.5 ± 141.0	25.29 ± 0.29	−1.45 ± 0.70	G
166	149.86594	2.37770	169.2 ± 16.3	24.49 ± 0.11	−1.28 ± 0.22	G
167	149.92056	2.38447	358.5 ± 17.7	23.79 ± 0.06	−1.66 ± 0.24	
168	149.85867	2.38496	906.0 ± 44.2	23.77 ± 0.05	−3.41 ± 0.49	
169	149.87639	2.40661	121.2 ± 13.5	24.65 ± 0.13	−0.84 ± 0.16	
170	149.97137	2.40845	639.9 ± 74.0	24.64 ± 0.13	−2.32 ± 0.60	
171	150.06847	2.40945	97.0 ± 18.2	25.18 ± 0.23	1.36 ± 0.15	
172	150.05676	2.41103	355.9 ± 38.4	24.59 ± 0.12	−1.61 ± 0.28	
173	149.87071	2.41723	114.8 ± 4.4	23.49 ± 0.04	−0.61 ± 0.09	G
174	150.37709	2.41963	99.0 ± 14.2	24.91 ± 0.17	−1.26 ± 0.20	G
175	150.38434	2.42810	430.4 ± 20.1	23.73 ± 0.05	−1.04 ± 0.24	
176	150.32805	2.42993	86.6 ± 9.2	24.60 ± 0.12	−0.67 ± 0.12	
177	150.32310	2.43075	115.1 ± 18.5	25.02 ± 0.19	−0.94 ± 0.19	
178	149.91571	2.43180	280.3 ± 34.9	24.73 ± 0.14	−0.63 ± 0.51	
179	150.38751	2.43257	835.0 ± 47.2	23.92 ± 0.06	0.15 ± 0.34	
180	150.36475	2.43840	97.4 ± 31.3	25.69 ± 0.42	−1.29 ± 0.27	
181	150.00362	2.43934	82.3 ± 10.6	24.81 ± 0.15	−2.29 ± 0.19	
182	150.18810	2.44029	320.6 ± 48.8	24.92 ± 0.18	−3.04 ± 0.64	
183	149.97662	2.44165	155.0 ± 17.4	24.65 ± 0.13	0.24 ± 0.21	
184	150.17717	2.44865	342.6 ± 61.9	25.08 ± 0.22	−3.96 ± 0.82	
185	150.10242	2.45022	154.5 ± 43.6	25.54 ± 0.36	−1.58 ± 0.41	
186	150.08235	2.46269	83.8 ± 32.2	25.87 ± 0.53	−1.37 ± 0.30	
187	150.05907	2.46698	102.1 ± 12.8	24.78 ± 0.15	−0.31 ± 0.18	

[a] Coordinates are in J2000. Candidates marked with the capital letter G are detected with GALEX, see text below.